Processing of Al_2O_3/SiC nanocomposites—part 2: green body formation and sintering

L.A. Timms*[,1], C.B. Ponton, M. Strangwood

IRC in Materials and School of Metallurgy and Materials, The University of Birmingham, Edgbaston, Birmingham B15 2TT, UK

Abstract

Pressure filtration was used to form green compacts from aqueous slurries of alumina with 5 vol.% silicon carbide. Green densities of 64%TD were achieved for slurries containing a 50 vol.% solids loading. Lower green densities were obtained for a very fine alumina due to the practical limits on maximum slurry solids loading when using finer powders. The samples were dried in a purposely built humidity cabinet to limit sample cracking. It was found that a higher consolidated layer permeability gave a higher initial drying rate. Near fully dense (99% TD) nanocomposites were produced, via pressureless sintering at 1900 °C. Poor sintered densities were obtained in the case of the fine alumina because of localised sintering of these low green density compacts. The required intra/inter-granular nanocomposite microstructures have been obtained for several different systems, with an average grain size of approximately 5 μm. Abnormal grain growth was noted for samples containing the larger particle size silicon carbide. This shows that a maximum particle size limit exists when selecting the powders for a 5 vol.% nanocomposite. © 2002 Elsevier Science Ltd. All rights reserved.

Keywords: Al_2O_3–SiC; Drying; Grain size; Nanocomposites; Pressure filtration; Sintering

1. Introduction

This paper forms the second part of a two-part investigation into the processing of Al_2O_3/SiC nanocomposites. Part 1[1] dealt with the aqueous processing of the starting powders to give well-dispersed slurries. This second part deals with the consolidation and densification of the nanocomposites and illustrates how carefully all processing steps need to be considered.

Typically, nanocomposites have been densified using hot pressing, using conventional powder processing, polymer precursor or sol-gel processing routes.[2] Pressureless sintering generally gives rise to lower density nanocomposites since the driving force for grain boundary movement is lower. Consequently, work has been carried out into the use of sintering aids.[3,4] More novel routes, such as spark plasma sintering,[5] have also been used. Here pressureless sintering was chosen as the densification route to investigate the practicality of applying conventional processing to nanocomposites. If successful, this would provide a basis for cost-effective scale-up to produce larger amounts of material.

Green body shaping of samples to be densified via a pressureless sintering route has, to date, been carried out using powder pressing techniques[6,7] or slip casting.[8] However, the work presented here concerns a new approach to the forming of Al_2O_3/SiC nanocomposites; namely pressure filtration. The major advantage in using pressure filtration is that it allows the powder particles to be kept in a liquid dispersing medium right up to the point of particle–particle contact during the consolidation step. The pressure applied during shaping means reduced forming times are necessary compared with slip casting. The equipment used is also very simple compared with equivalent techniques such as vacuum or pressure slip casting. Since no drying stage is necessary prior to consolidation, the electric double layer and/or steric repulsion forces are not removed, maintaining sol stability. If agglomeration is permitted, through drying, the advantages of using sub-micrometer particles are lost. Such inhomogeneities introduced into the powder compact are on a much larger scale than the primary

particles themselves, and will control ultimately the evolution of the microstructure during sintering.[9]

The basic nanocomposite microstructure consists of an alumina matrix with intra/inter granular silicon carbide particles. The smaller particles are found at intra granular locations and the larger particles in inter granular positions. It is to be expected that the larger particles will remain at grain boundary positions because their pinning effect is higher. This is because, in order to move past a particle, the grain boundary area must increase by a value proportional to the cross-sectional area of the particle.

Carroll et al.[10] studied the effects of second phase particle *size* on the microstructure of various Al_2O_3/SiC nanocomposite systems. Very fine silicon carbide was produced through a polymeric precursor route. The coarser powders were commercially produced sub-micron powders, with average particle sizes greater than 100 nm (H. C. Starck UF 15 and UF 45). No significant change in silicon carbide distribution was found for the different second phase particle size distributions, with similar mixed intra/inter granular microstructures produced after hot pressing at one temperature (1700 °C, 1 h) for all samples. This is not surprising since different size silicon carbide particles will be present on any given grain boundary prior to densification, and the movement of the grain boundary will be affected by all of the particles. For a given volume fraction of second phase there will be a higher number of individual particles, the finer the particle size. Consequently, the overall pinning effect on any given boundary, and thus the distribution of the silicon carbide, will be dependent on a combination of the size and number of particles. Zhang et al.[11] found that 0.6 μm particles inhibited grain growth more effectively than 2.7 μm particles, for the same volume fraction of second phase. In addition, several authors have noticed abnormal grain growth in material containing no silicon carbide particles.[12, 13] Carroll et al.[10] have also reported on the higher propensity for abnormal grain growth in monolithic alumina, compared with the composite. The pinning effect is also most likely responsible for the 'wavy' nature of the grain boundaries found in the nanocomposites, observed by several groups.[6,7]

The appearance of sub-grain boundaries, formed as a result of intra-granular particle induced dislocations have been reported by several groups[10,12,14] and is also contested by other workers.[15] However, the importance of such microstructural features must be understood to ascertain the plausibility of Niihara's[16] claims that matrix grain refinement is the reason for the very high strengths he obtained in these materials. This necessitates the removal of critical flaws that are larger than the alumina matrix grains. Carroll et al.[10] observed flaws in the size range 1–25 μm, due to the of silicon carbide agglomerates. Strength limiting crack-like voids are created in the alumina matrix around these flaws as a

result of elastic relaxation differences after cold pressing and/or differential sintering during the heat treatment stage. The size of the agglomerates was found to increase when using finer second phase powders due to increased difficulties in processing such fine powders, which naturally are so prone to agglomeration. It is important, therefore, to eliminate the processing flaws in these materials, to expose any nano-scale microstructural effects on properties.

2. Experimental procedure

Table 1 serves to remind the reader of the notation used for the slurries presented in the previous paper (Part 1[1]) on the aqueous processing of the nanocomposites. This notation will be used hereafter in the text. Additional information on the powders used is presented in Table 2.

2.1. Pressure filtration

The equipment used for forming 70 mm diameter discs via pressure filtration is shown in Fig. 1. The device was positioned upside down relative to that shown in the fig.

Table 1
Details of the slurry batches used to produce green samples

Slurry name	Alumina type	Silicon carbide type
SL/J	Alcan, RA207LS	H.C. Starck, UF15
SL/K	Baikalox, CR15	H.C. Starck, UF15
SL/L	Alcan, RA207LS	H.C. Starck, UF15
SL/M	Baikalox, CR15	H.C. Starck, UF15
SL/N1	Alcan, RA207LS	H.C. Starck, UF32
SL/N2	Alcan, RA207LS	H.C. Starck, UF45
SL/P	Alcan, RA207LS	H.C. Starck, UF15
SL/Q1	Alcan, RA207LS	ENEA
SL/Q2	Alcan, RA207LS	ENEA
SL/R	Alcan, RA207LS	–
SL/S	Alcan, RA207LS	H.C. Starck, UF15
SL/V	Alcan, RA207LS	H.C. Starck, UF32
SL/W	Alcan, RA207LS	H.C. Starck, UF45

Table 2
Manufacturers' data on the powders used

Powder	Surface area (m²/g)	Particle size, d_{50} (μm)
Alcan RA207LS	7.0	0.50
Baikalox CR15	15.0	0.40
H. C. Starck UF15	15.0	0.50[a]
H. C. Starck UF32	32.0	0.35[a]
H. C. Starck UF45	45.0	0.20[a]
ENEA	80.0	0.05[b]

[a] Average of values obtained from the literature.
[b] Obtained from TEM micrographs.

to allow the air in the system above the slurry to be expelled first. A fine pore size filter paper (2.7 μm, Whatman International Ltd, UK) was used to provide the primary resistance to the passage of the powder particles, to build up the initial compact layer of the green body. This was supported by a partially sintered stainless steel disc, having a mean pore size of 6 μm (Porvair Technology Ltd, UK). A typical load versus time trace is given in Fig. 2, showing that the maximum 'dwell' was applied via a low range cyclic load (19.2±0.1 kN; 5 MPa). The crosshead speed used for stages I–IV was 0.5 mm/min, and was 1 mm/min for stage V.
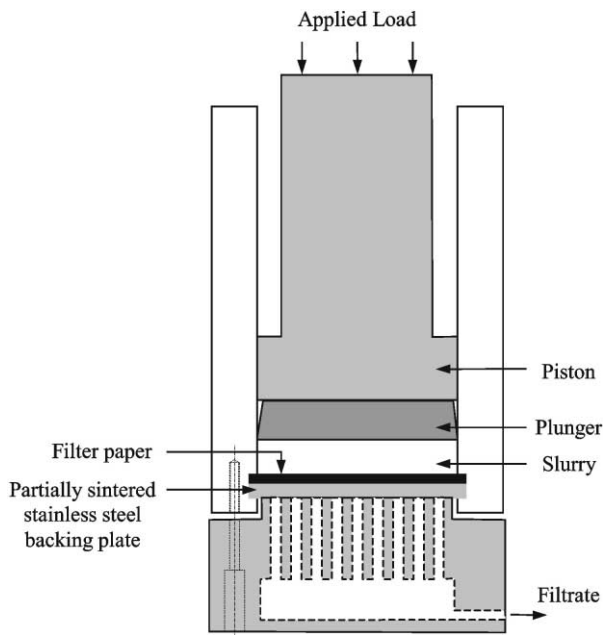

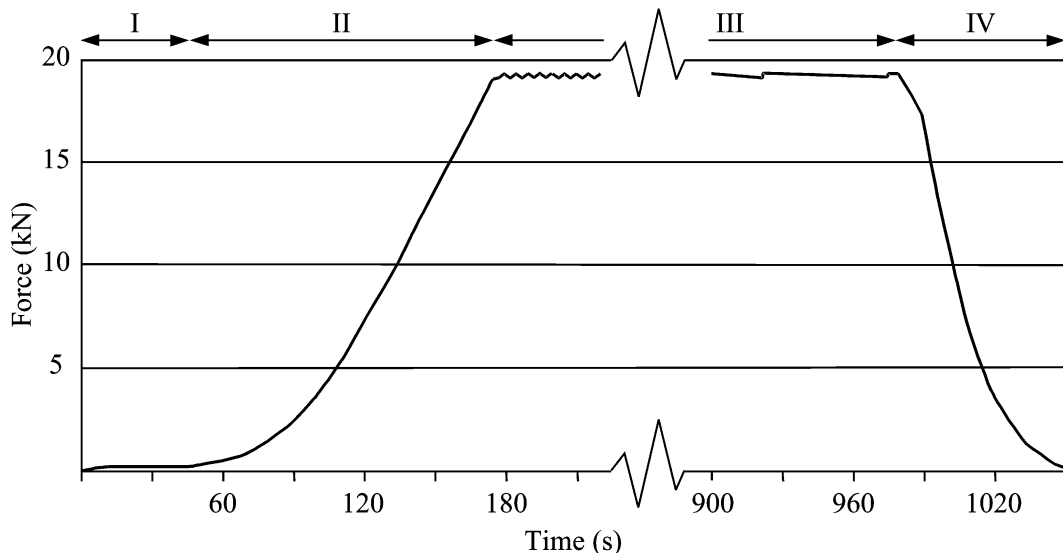Fig. 1. Schematic diagram of the pressure filtration equipment.

Early samples were dried in the laboratory under normal humidity conditions at room temperature. However, several of these samples developed drying cracks. Investigations were carried out to deduce the likely origin of such defects and ultimately a humidity cabinet was constructed for controlled drying of the discs. A saturated solution of sodium chloride in water was used to provide a high relative humidity (∼75% RH).

2.2. Heat treatment

Thermogravimetic analysis revealed the onset of the dispersant degradation to be around 320 °C, with complete decomposition by 540 °C. Consequently, a calcination treatment to 600 °C for 2 h was used to remove the polymer prior to sintering. Oxidation of the silicon carbide started at 800 °C, giving confidence that no significant oxidation of the second phase particles occurs during the calcination stage.

Pressureless sintering of the samples was carried out in a vacuum furnace (Lenton Thermal Designs Ltd, UK), backfilled with argon above 1000 °C. Samples were stacked into a graphite pot containing boron nitride powder to keep the samples separated from each other. A heating rate of 5 °C/min was used, with a 2 h dwell at the sintering temperature. Cooling was controlled at 10 °C/min until the minimum temperature measurable through pyrometer control was reached, followed by furnace cooling (with no power to the elements).

Initially different maximum temperatures were used to determine an optimum sintering temperature for the RA207LS/UF15 nanocomposites of 1900 °C. Alumina samples were sintered in air at 1600 °C with a 2 h dwell, using a heating and cooling rate of 5 °C/min.

Fig. 2. Typical load versus time profile for a pressure filtration run, with the individual stages marked at the top of the graph.

3. Results and discussion

3.1. Pressure filtration

For a disperse slurry (implies that n and α_c, defined below, are constant with respect to x), the thickness of the consolidated body is related to the filtration time by the following equation:[17]

$$\xi_c = \sqrt{\frac{2Pt}{\eta n \alpha_c}} \tag{1}$$

where ξ_c is the location of the suspension-consolidated layer interface, P is the hydraulic pressure drop over the system, t is time, η is the viscosity of the filtrate, α_c is the specific resistance of the consolidated layer (i.e. the resistance per unit thickness) and n (a system parameter) is given by:

$$n = \frac{(1 - x_p - \varepsilon_c)}{x_p} \tag{2}$$

where x_p and ε_c are the volume fraction of particles in the suspension and consolidated layer, respectively. The use of the equation for pressure filtration in the form given above assumes that the specific resistance of the stainless steel filter plate is negligible, compared with that of the consolidated layer.

Different volumes of slurry were used from selected batches to produce samples of different thickness', in order to check the validity of Eq. (1). Plots of ξ_c versus $t^{1/2}$ were then generated and linear regression analyses performed to find values for the specific resistance of the consolidated layer; refer to Table 3. The value for the specific resistance of the filter plate, α_m was calculated from manufacturers' data to be $\alpha_m = 1.39 \times 10^{10}$ m^{-2}. Therefore, the specific resistance of the filter plate, α_m is insignificant compared with the specific resistance's of the consolidated layers, α_c, supporting the assumptions made in quoting the equations at the beginning of this section. The values obtained for the RA207LS/UF15 system are in very good agreement with values obtained by Lange and Miller;[18] their results were for dispersed alumina slurries with a mean particle size of 0.5 µm. However, care must be taken when comparing values

for the specific resistance of the consolidated layer because the viscosity of the filtrate will be affected by the amount of polymer in solution.

A correlation was found between the time to reach maximum load (stage II time) and the values for the specific consolidated layer resistance for SL/S, SL/V and SL/W; refer to Table 3. The higher the resistance of the layer to the flow of the filtrate, the shorter the time to maximum pressure, as might be expected. The CR15/UF15 system (SL/K) has a very short stage II time, indicating a very high resistance to filtrate flow. The total time to form a sample for this slurry was 94 min, from an initial volume of 31 ml. This cannot be explained simply by the lower solids content of this slurry, since an RA207LS/UF15 sample prepared from an initial volume of 55 ml (giving a higher volume of filtrate than the SL/K sample) took only 23 min to form. The reasons for this are thought to be due to a high specific resistance of the consolidated layer for these samples, due to the finer particle size of the CR15 alumina. Furthermore, the higher dispersant content will act to increase the viscosity of the filtrate. The reader is reminded that $t \propto \alpha_c^2$ and η^2, from Eq. (1).

The stage II times for the SL/Q1 and SL/Q2 slurries were 167 and 192s, respectively. The latter is expected to have a higher value than for the systems already discussed since it is a flocculated slurry, and will thus contain a bimodal pore size distribution.[19] The larger pores allow easier flow of the filtrate, giving rise to lower specific consolidated layer resistance and shorter filtration times. The long time for the SL/Q1 system is a result of the large flow channels generated in the consolidated layer by the large silicon carbide agglomerates. Particle rearrangement to give more densely packed areas will also be inhibited around such agglomerates.

Interesting observations were made when the load cycle period of a dispersed system (such as SL/S) and a flocculated system (SL/Q2) were plotted against time. The results of the analysis are shown in Fig. 3. The dispersed system shows an abrupt increase in cycle period at the end of the filtration process as particle contact takes place in the final layer of slurry. A flocculated system shows a more gradual transition, indicative of a compressible consolidated layer. This compressibility is the result of the collapse of the flocculated particle structure, together with the movement of particles into open spaces.[20] Although the silicon carbide in the SL/Q1 system is highly agglomerated, the agglomerates are incompressible, acting like a single particle of the same size and so a similar curve results to that of a dispersed system.

3.2. Drying of green compacts

Problems were experienced with some samples fracturing during the sintering runs. Cracks were visible to

Table 3
Calculated specific resistance of the consolidated from plots of ξ_c versus $t^{1/2}$ and stage II times

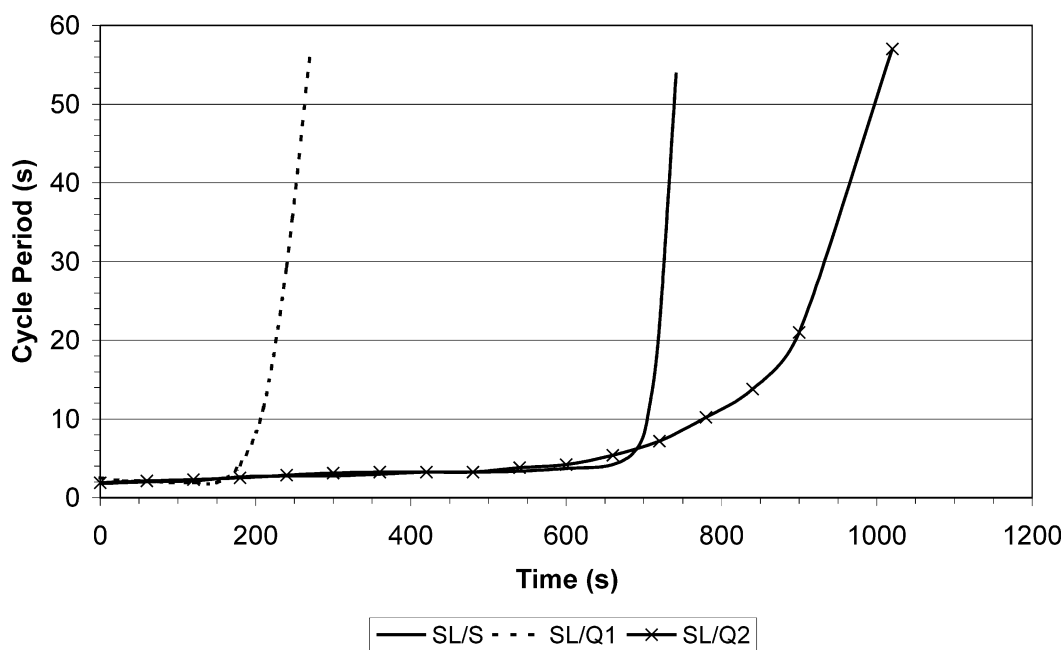| Slurry batch	$\alpha_c \times 10^{17}$ (m^{-2})	Stage II time (s)
SL/J	7.05	–
SL/S	7.50	127
SL/V	10.04	109
SL/W	9.29	118

Fig. 3. Variation in cycle period during Stage III of the pressure filtration run.

the naked eye in several samples before the calcination stage, with subsequent crack *extension* occurring during the heat treatment. Crack *formation* is therefore believed to take place during drying of the green compact. The problems experienced prompted the construction of a drying cabinet to establish a more controlled drying environment and to obtain drying data. The success rate for obtaining fully intact samples after sintering increased from 20% (3 out of 15) before the cabinet was used to over 50% (22 out of 42) following a controlled drying stage.

3.2.1. Drying curves

Typically, one sample from each slurry batch was weighed as a function of drying time in the cabinet. All samples were made from an original slurry volume of 31 ml. It is unlikely that a constant rate period (CRP)[2] will exist because the particles in the consolidated body will be in very close contact. Therefore, the initial masses of the discs should correspond to 100% saturation, assuming little drying had taken place between removal from the pressure filtration equipment to the drying cabinet. The 100% saturation mass was calculated from the final, dry green density, assuming the density of the filtrate to be 1 g cm^{-3}. Indeed, all samples weighed were between 99.7 and 99.8% saturated when put into the cabinet. The drying rate for the first falling rate period (FRP1) was calculated by performing linear regression analysis on the straight-line part of the drying curves.

Comparing the data for the specific consolidated layer resistance with the drying curve results revealed a correlation between the resistance and the FRP1 drying rate; namely a lower resistance gives rise to a higher drying rate. The only exception to this trend is the Q2 system. However, Q2 was a flocculated system and so it will be discussed separately.

The mechanism for drying in the first falling rate period is the flow of liquid through capillaries/pores to the surface where evaporation occurs. A decrease in specific resistance will allow a higher flow of liquid since the pore size of the compact will be larger. However, the capillary pressure that drives the flow will be lower and so verification of the most dominant contribution to the flow rate is required. If the pores are modelled as cylindrical tubes, Poiseuille's law can be used to examine the various parameters affecting the flow:

$$Q = \left(\frac{\pi r_p^4}{8 L_p \eta} \right) P_{lc} \qquad (3)$$

where Q is the flow rate of the liquid inside the pore, r_p is the radius of the pore, L_p is the pore length, η is the viscosity of the liquid and P_{lc} is the pressure difference. The magnitude of P_{lc} is related to the liquid-vapour interfacial energy, γ_{lv} and the radius of the meniscus, r_m by:

$$P_{lc} = -\frac{2\gamma_{lv}}{r_m} \qquad (4)$$

At the end of the CRP r_m is equal to r_p[21] and so substituting the expression for P_{lc} from Eq. (4) into Eq. (3) gives:

---

[2] The reader is referred to Scherer[20] for a review article on drying theory if the terms used in the text are unfamiliar.

$$Q = \frac{\pi \gamma_{lv} r_p^3}{4 L_p \eta} \qquad (5)$$

Eq. 5 shows that the flow rate dependency is reduced from r_p^4 to r_p^3 when the capillary pressure is taken into account. Nevertheless, the increase in flow rate and thus drying rate is still highly dependent on the size of the pore. The larger the pore size the lower the resistance to filtrate flow and so the observation that a lower specific cake resistance gives a higher drying rate is explained by this analysis. Although no allowance was made for evaporation inside the pores, the vapour pressure above a concave meniscus will increase with radius of curvature, according to the Thompson–Freundlich–Kelvin equation, resulting in higher drying rates for larger pores.

As already mentioned, the reason the Q2 system is an exception to the above trend is believed to lie with the fact that it is a flocculated system. The bimodal pore distribution will give rise to good filtrate flow during pressure filtration due to the larger pores. However, during drying, the larger pores will empty into the smaller pores,[21] and consequently the drying rate is determined ultimately by the smaller pores.

The final mass of the Q2/4 disc was noticeably higher than for the other samples. If the very fine ENEA silicon carbide is well dispersed, and not present as silicon carbide agglomerates, the amount of adsorbed water will be much higher for this system. Alternatively, if the silicon carbide is present as large agglomerates, as shown in the preceding paper (Part 1[1]), with no liquid inside the clusters, they will act as large particles. This will have the effect of simulating an alumina particle, from the point of view of water adsorption. Indeed, the Q1/3 disc had a similar final mass to that of the R/4 compact. These explanations are in agreement with the discussion on sol architecture presented in the previous paper (Part 1[1]).

3.2.2. Cracking behaviour

The control of the drying stage, using the drying cabinet, reduced the tendency for sample fracture. However, it did not completely eradicate the problem and so other possible contributory factors were investigated. Invasion percolation has been used to explain cracking after pressure filtration[18] due to the elastic recovery in the particle network on unloading. However, sample cracking was not found to be more pronounced in samples that experienced direct loading.

PTFE and stainless steel (polished to comparable surface finishes) were used as backing plates (refer to Fig. 1) to determine whether the plate material affected the propensity for crack formation. Since the backing plate remained in contact with the compact during the initial part of the drying period a constraint on shrinkage might be expected. This arises from frictional forces between the compact and the backing plate, which would be expected to be plate material sensitive; however, no such dependency was noted. Further discussion on cracking is presented in the Appendix.

3.3. Green density measurements

The averaged data for the green density of the discs (post calcination) are presented in Table 4. The data were calculated from mass and accurate dimensional measurements, performed with vernier callipers and a micrometer. At the commencement of the drying stage the mass ratio (percent dry mass) for the Q series slurries were notably higher than for the other systems, indicating a lower green density; this is confirmed by the data in Table 4. The table reveals a trend whereby a higher green density is obtained for a higher slurry solid content. Salomoni et al.[22] attribute this characteristic to the mechanism of the casting process itself, whereby the filtrate flow restricts the packing density because of the flow channels formed.

Table 4
Dimensions and densities of the green and calcined compacts

Original slurry	System type	Solid content of slurry (vol.%)	Green density (% TD)	Sintered bulk density (% TD)	Linear shrinkage (%)
SL/K	CR15/UF15	34.7	48.4±0.7	Sample 1: 71 Sample 2: 81	14, 18
SL/R	RA207LS	48.4	63.8±0.3	99.03±0.08	12.90
SL/J	RA207LS/UF15	49.8	64.1±0.2	97.68±0.30	13.93
SL/L		49.8	63.7±0.2	97.17±1.13	12.63
SL/P		49.5	63.3±0.3	98.03±0.54	13.51
SL/S		49.4	63.2±0.3	98.27±0.25	13.69
SL/N1	RA207LS/UF32	48.9	62.0±0.1	94.98±0.27	13.10
SL/V		48.3	62.0±0.0	94.34±0.19	13.44
SL/N2	RA207LS/UF45	48.4	61.9±0.1	94.50±0.47	13.15
SL/W		48.2	61.1±0.3	93.76±0.73	13.48
SL/Q1	RA207LS/ENEA	37.2	56.3±0.1	84.58±0.98	13.44
SL/Q2		38.6	54.1±0.1	98.97±0.12	17.49

Aslan et al.[8] used heterocoagulated and polydispersed sols to prepare slurries at relatively low solid contents (30 vol.%), which gave rise to green densities in the range 56–60% TD, via slip casting. Work by Assmann et al.[23] produced green densities of 62% TD from slurries prepared at higher solids loading of 47 vol.%. However, in the present work slurries prepared at 50 vol.% solids produced green bodies at up to 64% TD. The attainment of higher green densities is more critical when densification via pressureless sintering is used since diffusion is not aided by the application of external pressure as, for example, in the case of hot pressing.

The CR15 system exhibits a particularly low green density, which can be attributed to the fine alumina particle size, as well as to its initial solids loading. The CR15 alumina has also been shown to contain hard agglomerates, having a particle morphology that will be detrimental to the packing process (the reader is referred to Part 1[1] of this two-paper investigation).

3.4. Pressureless sintering

3.4.1. Density and shrinkage profiles

The bulk density, true density and percentage of open porosity versus temperature profiles for the CR15/UF15 system are shown in Fig. 4. The bulk density values for the CR15 based system are very low and exhibit a sharp decrease between 1700 and 1750 °C, which is reflected in the open porosity values. This is believed to be a consequence of the high sinter-activity of the alumina powder and the more open packing of the green sample. Areas of closer packed particles will densify readily due to the high surface area of the powder, leaving less dense zones

in-between. It is quite possible that defects will arise in these zones from the fracture of superficial necks, manifesting in the rise in interconnected porosity observed.

Fig. 5 shows a gradual decrease in porosity for the RA207LS/UF15 system, as a function of temperature. There is a minimum in the true density, accompanied by a drop in the bulk density at this point. Below 1500 °C sintering is taking place but the amount of open porosity diminishes, however, the pores still remain interconnected to the surface and so the true density is very close to the theoretical value. As the temperature increases the pore networks become discontinuous and the proportion of closed porosity rises, reducing the true density value. Further sintering and grain growth eliminates the closed porosity and the true density values rise, accordingly.

The values reported in the literature for pressureless sintered Al_2O_3/SiC nanocomposites range from 94.0% TD to 98.5% TD, at 1800 °C. However, Stearns et al.[6] reported a density of 99% TD after a heat treatment for 2 h at 1700 °C. The use of temperatures as high as 1900 °C has not been reported in the literature for the pressureless sintering of 5 vol.% Al_2O_3/SiC nanocomposites. Assmann et al.[23] have reported on the use of temperatures as high as 1950 °C to densify nanocomposites with 10 vol.% silicon carbide or higher. However, no improvements in density were achieved above 1880 °C, with a maximum density of 80% TD being achieved for 25 vol.% composites.

The density and shrinkage data obtained in the present study are presented in Table 4. The density values for the RA207LS/UF15 system are in good agreement with those found in the literature. Excellent results were obtained for the nanocomposite prepared with the ultra
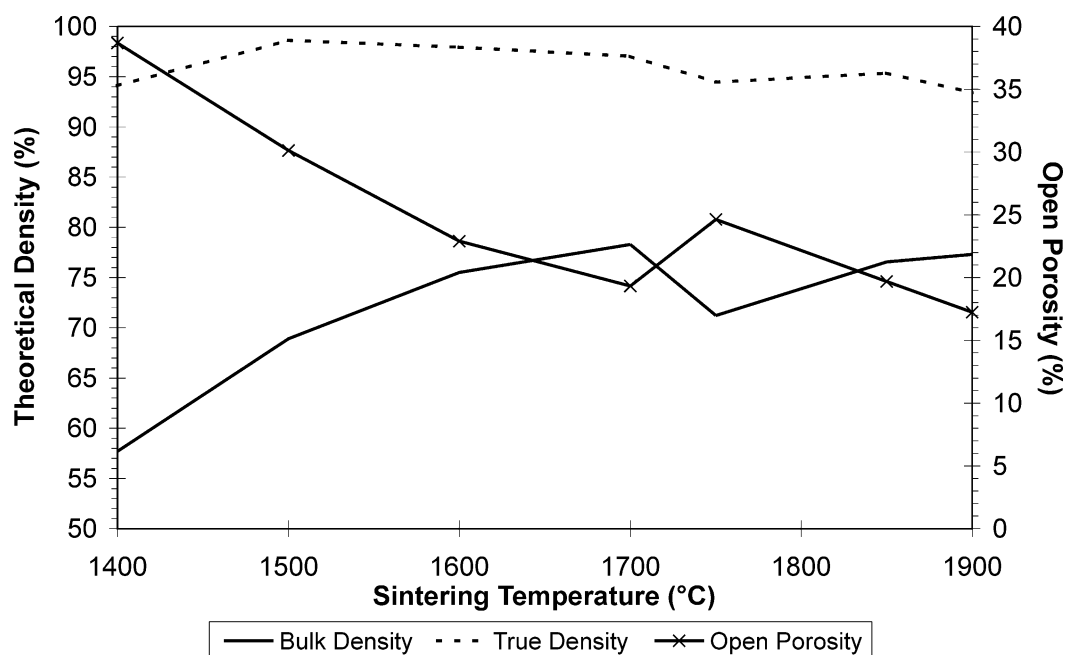

Fig. 4. Bulk density, true density and percentage open porosity as a function of temperature for the CR15/UF15 nanocomposite.
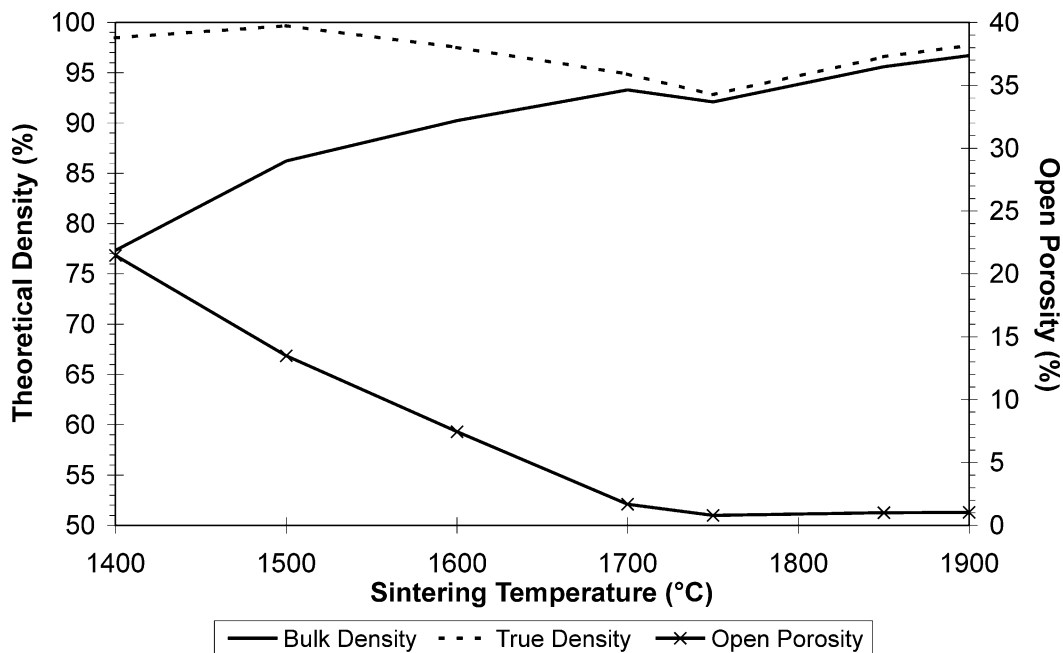
Fig. 5. Bulk density, true density and percentage open porosity as a function of temperature for the RA207LS/UF15 nanocomposite.

fine ENEA silicon carbide, processed at low pH (SL/Q2), whilst the system processed at high pH shows poor results due to extensive silicon carbide agglomeration. The silicon carbide agglomerates effectively stabilise the pores, since the second phase powder does not sinter at the temperatures used to densify the nanocomposites. The results for the finer H. C. Starck silicon carbide composites indicate a higher retardation in densification, compared with the UF15 composites.

The CR15/UF15 system shows very poor results due to the poor density in the as-calcined condition. The large difference in the data for the two samples measured are believed to be a consequence of the neck fracture mechanism already discussed at the beginning of this section.

The shrinkage values for the nanocomposites are higher than that for the monolith. This is due to the reduced contact between alumina grains prior to sintering, as a result of the presence of the silicon carbide particles.

3.4.2. High temperature reactions during sintering

X-ray diffraction of the sintered nanocomposites confirmed the presence of alumina and silicon carbide, although the major peaks for the second phase were, at the most, three times the background intensity. The ENEA silicon carbide gave rise to peak broadening due to the fine particle size of this powder. No amorphous phases were detected.

A thin layer of material became detached from some samples on removal from the graphite sintering pot. SEM examination revealed a porous layer, extending approximately 20 μm beneath the surface, shown in Fig. 6. The original white colouration of the boron

nitride powder bed was also found to change to green at temperatures above 1850 °C. X-ray diffraction of the powder bed revealed the presence of some aluminium nitride (AlN) and a trace of boron carbide (the stoichiometry of the boron carbide was difficult to determine due to the size of the peaks). The predominant gaseous species that can form at the high temperatures used in the present work are SiO, CO, Al_2O_3 and Al.[23] Therefore, it is likely that the gaseous aluminium is responsible for the formation of AlN in the powder bed.

Nieto et al.[24] has reported on the following reaction being responsible for the occurrence of a porous layer in Al_2O_3/SiC composites sintered in an argon atmosphere
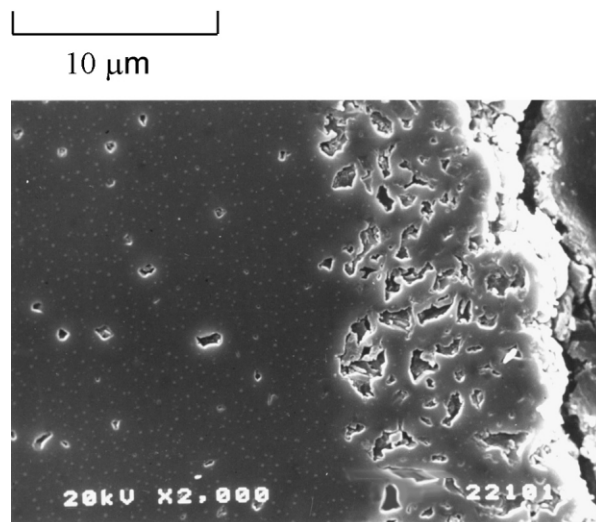

Fig. 6. SEM micrograph showing a porous surface layer in an RA207LS/ UF15 nanocomposite sintered at 1900 °C, 2 h.

$$SiC_{(s)} + O_{2(g)} \rightarrow SiO_{(g)} + CO_{(g)} \qquad (6)$$

A combination of this reaction, along with the loss of Al_2O_3 and Al in their gaseous form is believed to generate the porous layer witnessed in the present work. The generation of $CO_{(g)}$ may also inhibit densification if entrapped in pores after closure.[25] This may explain the reduced bulk densities for the finer H. C. Starck powders, due to their increased surface area for the above reaction. However, the ENEA powder, despite having the highest surface area, does not follow this trend, exhibiting the highest sintered density (SL/Q2). Nevertheless, since the particles are finer, the proportion of particles lying on grain boundaries at pore closure may be significantly reduced. Once inside the alumina grains, the above reaction will be greatly inhibited, since the diffusion of oxygen through the alumina lattice is greatly reduced compared with that along the grain boundaries.

3.5. General discussion on the processing and microstructure of Al_2O_3/SiC nanocomposites

Fig. 7 shows the typical microstructural features of the RA207LS/H. C. Starck SiC nanocomposites and the RA207LS/ENEA nanocomposite processed at low pH, as revealed by transmission electron microscopy. The actual system shown is the RA207LS/ENEA nanocomposite processed at low pH and revealing a characteristic intra/inter-granular microstructure. The RA207LS/ENEA systems processed at low and high pH will hereafter be referred to as RA207LS/ENEA$_l$ and RA207LS/ENEA$_h$. The change in Al_2O_3/Al_2O_3 grain boundary morphology caused by silicon carbide particles being present at the grain boundary is evident, through the creation of 'wavy' interfaces, as opposed to the typical straight boundaries normally observed. Fig. 8 shows a higher magnification of a wavy interface; such features have been reported by other workers.[6,7]

The typical microstructure for the RA207LS/ENEA$_h$ system (Fig. 9) reveals alumina grains without inter-granular or intragranular silicon carbide. This observation is expected from the previous discussion on sol architecture in the previous paper (Part 1[1]), as is the presence of silicon carbide agglomerates, resulting from the very poor dispersion in this material. Such agglomerates were indeed observed; an example of which is given in Fig. 10. These features act to stabilise pores, by limiting grain boundary movement, and explain the marked difference in final densities between the RA207LS/ENEA$_h$ and RA207LS/ENEA$_l$ composites.

Fig. 11 shows the typical microstructure of the CR15/UF15 system. The alumina grains are very thick and so appear dark, since suitable thinning of the alumina grains was not possible because of the high porosity of this sample. This is because when the 'necks' between alumina

Fig. 7. TEM micrograph showing the typical microstructure of the RA207LS/ENEA nanocomposite processed at low pH.

Fig. 8. TEM micrograph showing the effect of grain boundary silicon carbide on the morphology of the interface in an RA207LS/ENEA nanocomposite processed at low pH. The presence of a sub-grain boundary is also evident.

Fig. 9. TEM micrograph showing the typical microstructure of the RA207LS/ENEA nanocomposite processed at high pH.

Fig. 11. TEM micrograph showing the typical microstructure of the CR15/UF15 nanocomposite.

Fig. 10. TEM micrograph showing pore stabilisation by silicon carbide agglomerates in the RA207LS/ENEA system processed at high pH. The remains of a silicon carbide agglomerate can be clearly seen in the pore in the top-left part of the micrograph.

grains are thinned they cause parts of the sample to drop out of the centre of the specimen. The curved area in the top right of the micrograph is indicative of such an over-thinned region. The minimum particle separation in this material prior to sintering, taking into account the calcined density and modelling the system on a face-centred cubic arrangement of 0.1 μm diameter particles, should be 15.2 nm. However, measurement of the pore in the bottom left of Fig. 11, reveals a pore size of at least 6 μm. This indicates that severe localised sintering has taken place. This is not surprising since regions of alumina to alumina particle contact will sinter readily at the temperatures used for densification, due to the high sinter-activity of this powder. As coarsening proceeds the curvature of the resulting sintered areas will reduce and therefore be less able to pass second phase particles, especially where large (0.5 μm) silicon carbide is utilised. The sintering alumina regions may act to 'sweep' silicon carbide particles along in their path and so clusters of second phase particles are to be expected; refer to Fig. 12.

The colloidal approach of using a polydispersed system to produce the required dispersion has been demonstrated for RA207LS/H. C. Starck SiC systems since similar microstructures to that shown in Fig. 7 were obtained for these systems. However, small defects in the form of silicon carbide agglomerates/clusters were witnessed for the finer H. C. Starck powders, as shown in Fig. 13, in agreement with Carroll et al.[10] Indeed, the application of a
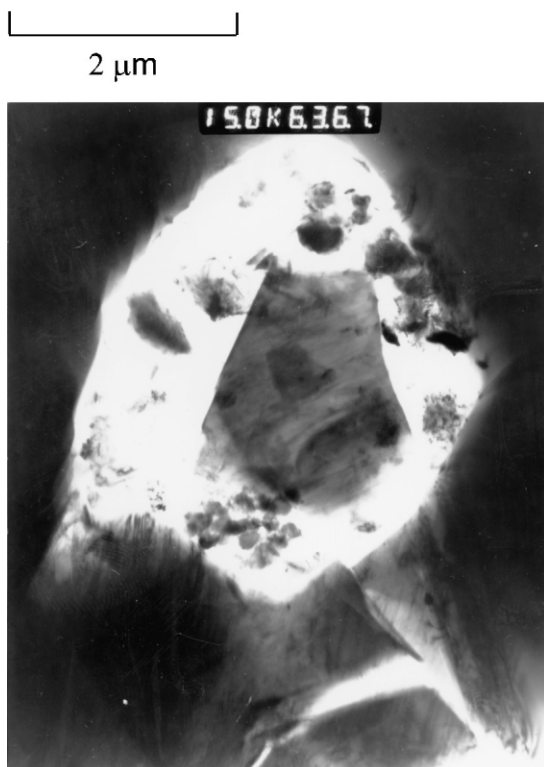
Fig. 12. TEM micrograph showing the clustering of silicon carbide inside the central void area, by the movement of grain boundaries in the CR15/UF15 nanocomposite.

like-charged particle dispersion route to the processing of the *very fine* second phase particles from ENEA has been shown to produce very undesirable features. Large clusters from the original dry powder are not broken down (refer to Part 1[1]), yielding sintered microstructures with silicon carbide free alumina grains (Fig. 9) and large pores (Fig. 10). There were, however, no significant second phase clusters in the RA207LS/ENEA$_l$ system, despite the very fine particle size of the ENEA powder. This suggests that a heterocoagulation route, similar to that developed here, is required to generate well dispersed nanocomposite sols with very fine second phase dispersions.

Grain size data for the nanocomposites were obtained by measuring the largest dimension across grains from five or six TEM micrographs taken at a low magnifica-

tion (5000×); refer to Table 5. The CR15/UF15 and RA207LS/ENEA$_h$ composites were not included in this analysis due to practical limitations, such as insufficient electron transparency, already discussed. The reason for the low number of grains counted for the RA207LS/ UF15 system is that the micrographs contained large grains that could not be measured with certainty. Therefore, the maximum and average grain size figures will be an underestimate of the actual values.

The average grain size decreases with decreasing nominal second phase particle size, with a marked effect for the ENEA system. Considering the minimum grain size results also suggests that finer second phase dispersions are more effective at producing a finer nanocomposite microstructure. From the work by Aksay and Schilling,[26] a smaller grain size would be expected for the RA207LS/ENEA$_l$ system since it is a flocculated sol. Dispersed systems will form larger grains because the domain size is larger. It is suggested that the concept of domains will still apply here since, for an even distribution of the second phase, all grain growth retardation effects will be the same throughout the individual domains in the material.

The majority of the silicon carbide is located ultimately within the alumina grains for the RA207LS/ENEA$_l$ system (Fig. 7). However, suitable retardation of the densification process has obviously occurred. Comparing the H. C. Starck systems, there are more likely to be silicon carbide free grain boundaries in the case of a larger silicon carbide particle size (at constant volume fraction). Therefore, the grain size would be higher in these regions, giving rise to a larger average grain size. Work by Zhang et al.[11] supports this argument, since they observed more effective inhibition of grain growth in composites containing 0.6 μm particles, compared with 2.7 μm particles. The situation will be exacerbated by the formation of silicon carbide clusters, as shown in Fig. 13.

It is not possible to apply grain size limiting equations, such as those by Zener[27] and Stearns and Harmer.[28] This is because, for nanocomposites with a low volume fraction of second phase, much longer times are required to reach the limiting grain size than those used for a typical sintering run.[29] Dilatometry studies may help to determine reduced sintering temperatures, with extended dwell

Table 5
Grain size measurements for the nanocomposites with high sintered density

Nanocomposite system	No. grains measured	Minimum grain size (μm)	Maximum grain size (μm)	Average grain size (μm)
RA207LS/UF15	26	2.0	(11.0)[a]	(5.5)[a]
RA207LS/UF32	47	2.0	14.0	5.4
RA207LS/UF45	50	2.0	9.0	5.3
RA207LS/ENEA$_l$[b]	50	1.6	10.0	4.8

[a] See comments in the text.
[b] Subscript implies system processed at low pH.

Fig. 13. TEM micrograph showing a small SiC cluster in an RA207LS/UF32 nanocomposite, showing absence of amorphous grain boundary phase(s).
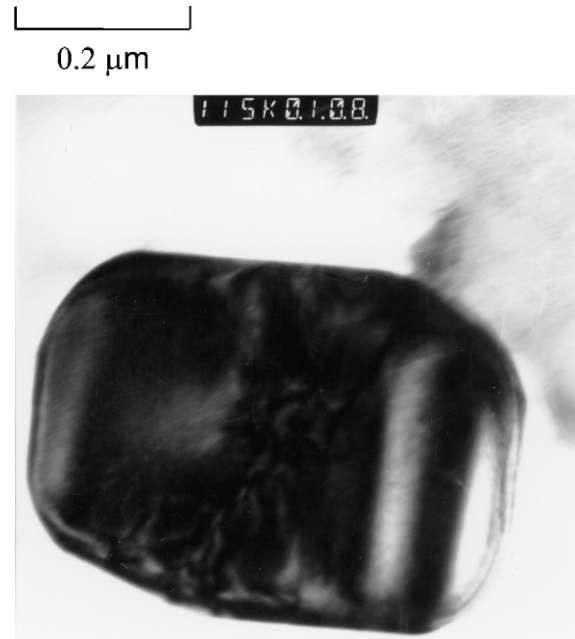

Fig. 15. High magnification TEM micrograph of an intragranular silicon carbide particle in the RA207LS/UF15 system.

Fig. 14. High magnification TEM micrograph of an Al_2O_3/Al_2O_3 grain boundary in the RA207LS/ENEA system processed at low pH.
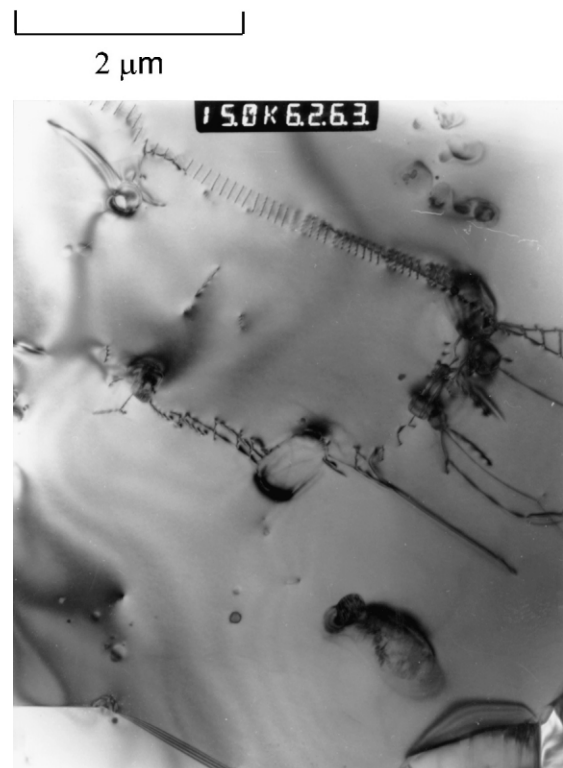

Fig. 16. TEM micrograph showing dislocation arrays and sub-grain boundary formation in an RA207LS/UF32 nanocomposite.

Fig. 17. TEM micrograph showing the area below the micrograph in Fig. 16, with a common region shown in both micrographs.

Fig. 19. TEM micrograph showing extensive sub-grain boundary formation in an RA207LS/ENEA nanocomposite processed at low pH.

Fig. 18. TEM micrograph showing sub-grain boundary and associated dislocations in an RA207LS/UF45 nanocomposite.

times, and reduce the maximum grain size of the nanocomposites. This approach may be particularly fruitful for the case of the RA207LS/ENEA$_1$ system, since the density/temperature profile was not optimised.

Fig. 14 and 15 show high magnification TEM micrographs of the grain boundaries, showing no evidence of the formation of amorphous phases, as witnessed by Schmid et al.[30] The intragranular silicon carbide particle in Fig. 15 is approximately 500 nm in size. Hot pressed microstructures have been reported to contain intragranular silicon carbide of generally no more than 200 nm.[16] Clearly, considerable grain boundary mobility occurs at the high sintering temperatures used in the present study, due to atom movement obeying Arrhenius-type behaviour.

Dislocation pile-ups and the formation of sub-grain boundaries were noted in the nanocomposites prepared from UF32, UF45 and ENEA powders, as shown in Fig. 8, 16–19. The appearance of sub-grain boundaries has been reported as a typical microstructural feature in Al$_2$O$_3$/SiC nanocomposites by several groups.[10,12,14] Sub-grain boundaries appear to form in areas of high second phase density. If the number of second phase particles per grain is high enough the sub-grain boundaries form links between the inclusions, traversing the whole grain, as shown in Fig. 19. At constant volume fraction of silicon carbide, it is proposed that a coarse second phase powder (e.g. UF15) will not provide

sufficient local stresses within the alumina grains to propagate the sub-grain boundary. This is simply due to the reduced number of second phase particles within the grains and explains why no sub-grain boundaries were noted in the RA207LS/UF15 material. Certainly, microstructural refinement of the matrix grains in the RA207LS/ENEA$_1$ nanocomposite has taken place through the incorporation of silicon carbide particles, in agreement with the work of Niihara.[16]

4. Fracture strength

Fracture strength data were obtained from four-point bend tests (sample volume normalised to 400 mm^3 with top and bottom roller separation of 20 and 40 mm, respectively). A maximum strength value of 520 MPa was determined for the RA207LS/ENEA$_1$ system, but with no obvious improvement over that of alumina alone, with a maximum strength of 470 MPa recorded for RA207LS. The Weibull modulus was increased from 8.0 for RA207LS to 13.5 for the RA207LS/UF32 material, indicating the most uniform microstructure in terms of critical flaw size. Fracture strengths were limited by the occurrence of abnormal grain growth (UF15 composite), remnant porosity (UF32 and UF45 composites), and defects associated with pressure filtration (RA207LS/ENEA$_1$ system; refer to Appendix, Fig. A5). A superior surface finish was obtained for the nanocomposites during specimen preparation, in agreement with other workers.[7,31,32] However, this was not found to be critical for the fracture strength.

5. Conclusions

Pressure filtration allows the dispersed sol characteristics to be retained to the point of consolidation, and avoids problems associated with the formation of hard agglomerates when drying slurries; for example, prior to dry pressing. The technique has been used here to produce alumina–5 vol.% silicon carbide nanocomposites with green densities of up to 64% TD. Low green densities are obtained as a result of the practical limits on maximum slurry solids loading when using finer powders.

The occurrence of post-forming drying defects can be reduced by controlling the water evaporation rate in a humidity cabinet, with the initial drying rate being dependent on the permeability of the green compact.

Pressureless sintering at 1900 °C gave near fully dense (99% TD) nanocomposites. Localised sintering took place in the case of the very fine CR15 alumina powder to give very low sintered densities. High sinter-active powders are normally attractive when using pressureless sintering, but problems in processing these powders lead to low green densities in the present work.

The required intra/intergranular nanocomposite microstructures have been obtained for the RA207LS/UF32, RA207LS/UF45 and RA207LS/ENEA$_1$ materials, with an average grain size of approximately 5 μm. However, a change from a polydispersion approach to a hetero-coagulated system had to be adopted for the colloidal processing of the finer silicon carbide, as discussed in Part 1[1] of this two-part investigation. Abnormal grain growth was noted for samples containing the larger UF15 silicon carbide. This shows that a maximum particle size limit must be applied when selecting the powders, since the number of particles (at a constant volume fraction of second phase) reduces with increasing particle size. This lowers the potential for grain boundary pinning during sintering, and hence, for limiting grain growth.

The morphology of the grain boundaries is affected by the presence of the silicon carbide, giving rise to grain boundary curvature. Dislocation arrays and sub-grain boundaries are common features, with obvious grain refinement being obtained in the RA207LS/ENEA$_1$ nanocomposite.

In summary, Al$_2$O$_3$/SiC nanocomposites have been prepared successfully via a conventional processing and pressureless sintering route. However, until processing defects can be eliminated more effectively, improved fracture strengths cannot be realised and the true nanocomposite strengthening mechanisms exposed.

Acknowledgements

Appendix. Cracking behaviour—proposed mechanisms

Fig. A1 shows the different types of cracking behaviour observed, with each type occurring in discs prepared from different original slurries. For example, the severe cracking shown in Fig. A1(d) was observed in a sample from the SL/L and SL/N1 slurry, as well as from the SL/P slurry (shown). Some samples also cracked, to form two pieces, in an approximate straight line along a diameter. The cracking behaviour is believed to have resulted from packing defects introduced by drying stresses. In several instances, cracks could be observed, by the naked eye, in the green samples after drying. Fig. A2 shows one such sample; (a) indicates the appearance after calcination but prior to sintering.
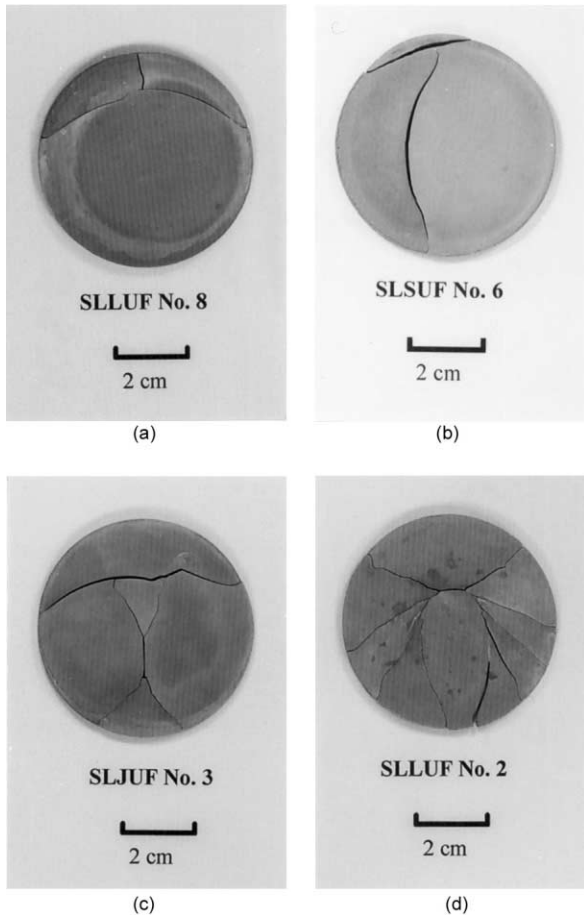
Fig. A1. Various cracking formations that evolved during sintering.

Fig. A2. Diagram showing the drying cracks and the corresponding sintered sample.

Since the compact is 100% saturated initially, evaporation will lead to the development of stresses between saturated and unsaturated areas immediately after formation. It is convenient, for the purposes of discussion, to group the cracks observed in the sintered bodies (shown in Figs. A1 and A2) into different types. A consideration of cracking in the circular plane is implied; however, the same mechanisms will apply across the thickness of the discs. It can be argued that cracking in the through thickness plane is far less likely as the cumulative capillary pressure will be lower.

I. Radial; nominally straight cracks, formed at approximately right angles to the circumference with some propagating to join other cracks in the sample. Examples are Figs. A1(a) and (d) and A2(b).

II. Circumferential; arc shaped cracks. Examples are shown in Fig. A1(a)–(d).

III. Central; nominally straight cracks formed along a diameter. These cracks may exist over part of a diameter, as in Fig. A1(c) or over a whole diameter, as mentioned at the beginning of the appendix.
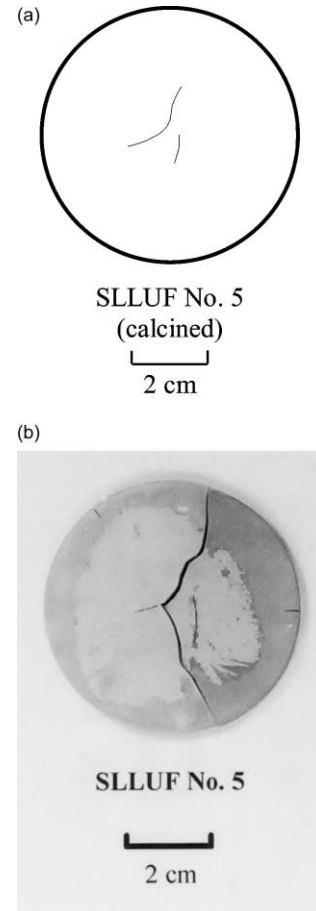
The radial cracking behaviour is thought to be due to the presence of an irregular drying front, shown schematically in Fig. A3. This mechanism would support the relatively straight path of the crack (macroscopically
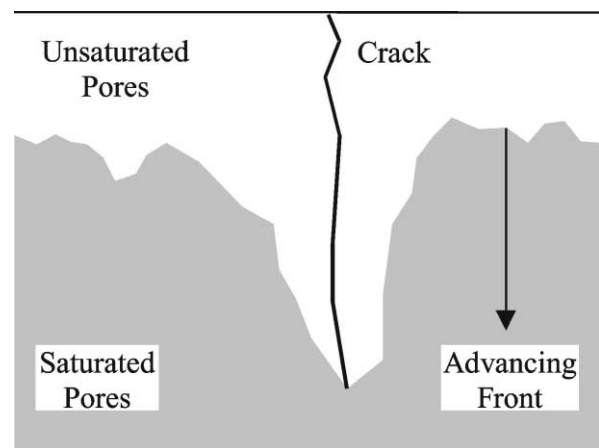

Fig. A3. Schematic diagram of the possible mechanism for the formation of radial cracks.
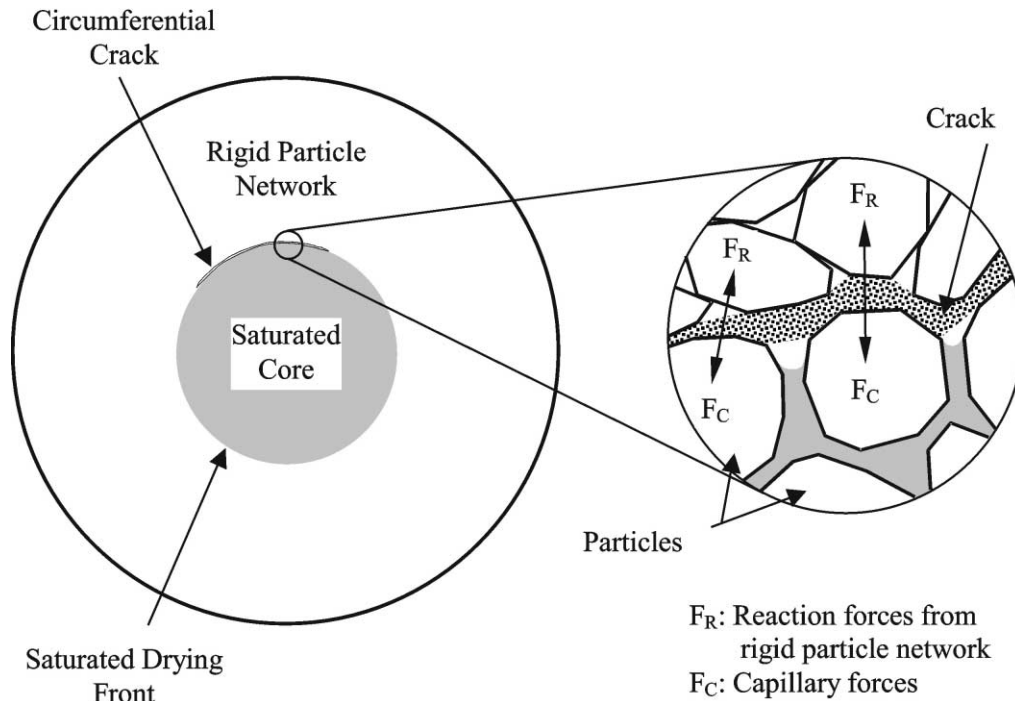
Fig. A4. Schematic diagram of the formation of circumferential drying cracks.
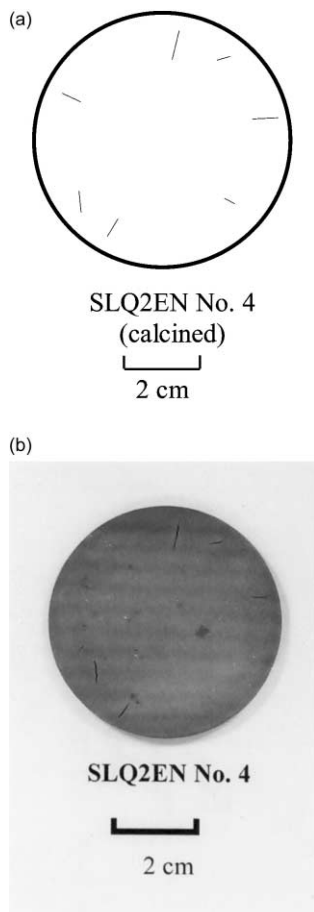

Fig. A5. Schematic diagram of the short cracks observed in compacts made from the SL/Q2 slurry.

speaking) since the pores near the newly formed surface will empty preferentially due to shorter fluid flow paths.

Circumferential cracks form due to the tension set up as a result of the negative pressure inside the pores in the receding saturated zone and the rigid network of empty pores; refer to Fig. A4. Consequently, the cracks formed show a more curved morphology. This behaviour is somewhat analogous to the phenomenon of differential sintering; for the case of a lower density region inside a higher density matrix, as reported by various workers such as Lange and Metcalf.[9] Central cracks are thought to originate at the point where the saturated drying front disappears. The normal shrinkage associated with the disappearance of the saturated volume will be prohibited by the surrounding rigid particle network and so packing defects will arise, which may form cracks on sintering.

Since radial cracks are brought about by an irregular drying front, the control of such defects is dependent on the local pore size distribution. Consequently, it is difficult to suppress such features once the compact has been formed. Circumferential defects can be avoided by slowing the advance of the saturated drying front, to allow particle rearrangement to take place. This rearrangement is thought to strengthen the unsaturated volume through an increase in the number of particle contacts supporting the drying stress. Chiu et al.,[33] have shown that sedimentation effects play an important role in increasing the critical thickness that gives rise to crack formation in films. Particle rearrangement can be realised practically by reduced drying rates; and has been

shown to improve the proportion of non-fractured sintered samples in the present work. Although this will not prevent central defects forming, it is thought to limit their length. It may then be possible for closure on sintering, since the defects will be surrounded by a shrinking network. In practice, control of the drying stage did give rise to improvements in the cracking behaviour, through the prevention of circumferential and central cracks. Of the samples that remained intact throughout sintering, some did still contain radial cracks, which supports the above discussion on formation mechanisms.

It is interesting to note that cracks may well be arrested during sintering, as shown in Figs. A1(d) and A2(b). This is due to the effect of a shrinking network of particles around a crack tip.

Aside from defects caused by drying, air inclusions on the millimetre scale were noted in the higher viscosity slurries, especially for the SL/Q2 system; refer to Fig. A5(a). The green samples produced contained small cracks several millimetres in length, of random orientation and with none intersecting the sample circumference. Therefore, they are not considered to be the radial cracks already discussed. Lange and Miller[18] proposed that air bubbles collapse and are broken into much smaller voids on consolidation. On drying, the surrounding capillary pressure will serve to open the lenticular region of poor packing, to form a crack. The initial cracks are unable to heal under the pressureless densification heat treatment and are clearly visible in the sample surface; refer to Fig. A5(b).

References

1. Timms, L. A. and Ponton, C. B., Processing of Al_2O_3/SiC nanocomposites—part 1: aqueous colloidal processing. *J. Eur. Ceram. Soc.*, **22**, 1553–1567.
2. Sternitzke, M., Review: structural ceramic nanocomposites. *J. Eur. Ceram. Soc.*, 1997, **17**, 1061–1092.
3. Jeong, Y. K. and Niihara, K., Microstructure and mechanical properties of pressureless sintered Al_2O_3/SiC nanocomposites. *Nanostruct. Mater.*, 1997, **9**, 193–196.
4. Jeong, Y. K., Nakahira, A. and Niihara, K., Effects of additives on microstructure and properties of alumina–silicon carbide nanocomposites. *J. Am. Ceram. Soc.*, 1999, **82**(12), 3609–3612.
5. Gao, L., Wang, H. Z., Hong, J. S., Miyamoto, H., Miyamoto, K., Nishikawa, Y. and Torre, S. D. D. L., Mechanical properties and microstructure of nano-SiC–Al_2O_3 composites densified by spark plasma sintering. *J. Eur. Ceram. Soc.*, 1999, **19**, 609–613.
6. Stearns, L. C., Zhao, J. and Harmer, M. P., Processing and microstructure development in Al_2O_3–SiC 'nanocomposites'. *J. Eur. Ceram. Soc.*, 1992, **10**, 473–477.
7. Walker, C. N., Borsa, C. E., Todd, R. I., Davidge, R. W. and Brook, R. J., Fabrication, characterisation and properties of alumina matrix nanocomposites. In *British Ceramic Proceedings, No. 53: Novel Synthesis and Processing of Ceramics*, ed. F. R. Sale. The Institute of Materials, London, 1994, pp. 249–264.
8. Aslan, M., Dörr, Naß, R. and Schmidt H., Microstructural development and mechanical properties of pressureless sintered Al_2O_3/SiC composites. In *Proceedings of the International Conference Ceramic Processing Science and Technology*, 11–14 September. Friedrichshafen (Bodensee), FRG, 1994, pp. 665–669.
9. Lange, F. F. and Metcalf, M., Processing related fracture origins: II. *J. Am. Ceram. Soc.*, 1983, **66**(6), 398–406.
10. Carroll, L., Sternitzke, M. and Derby, B., Silicon carbide particle size effects in alumina-based nanocomposites. *Acta Mater.*, 1996, **44**(11), 4543–4552.
11. Zhang, Y. F., Deng, Z. Y., Shi, J. L., Mao, Y. Q. and Guo, J. K., Microstructure and mechanical properties of SiC particle reinforced Al_2O_3 matrix composites. *J. Mater. Sci. Lett.*, 1996, **16**, 1927–1931.
12. Xu, Y., Zangvil, A. and Kerber, A., SiC nanoparticle-reinforced Al_2O_3 matrix composites: role of intra- and intergranular particles. *J. Eur. Ceram. Soc.*, 1997, **17**, 921–928.
13. O'Sullivan, D., Poorteman, M., Descamps, P., Cambier, F., Leriche, A. and Thierry, B., Optimisation of alumina—silicon carbide dispersions and the fabrication of nanocomposite ceramic materials. In *Key Engineering Materials*, 99–100. Trans Tech Publications, Switzerland, 1995, pp. 247–256.
14. Niihara, K. and Nakahira, A., Strengthening and toughening mechanisms in nanocomposite ceramics. *Ann. Chim. Fr.*, 1991, **16**, 479–486.
15. Fang, J., Harmer, M. P. and Chan, H. M., Evaluation of sub-grain formation in Al_2O_3/SiC nanocomposites. *J. Mater Sci.*, 1997, **32**, 3427–3433.
16. Niihara, K., New design concept of structural ceramics: ceramic nanocomposites. *J. Ceram. Soc. Jpn. Int. Ed.*, 1991, **99**, 945–952.
17. Aksay, I. A. and Schilling, C. H., Mechanics of colloidal filtration. In *Advances in Ceramics*, Vol. 9, *Forming of Ceramics*, ed. J. A. Mangels and G. L. Messing. Am. Ceram. Soc. Inc., 1984, pp. 85–93.
18. Lange, F. F. and Miller, K. T., Pressure filtration: consolidation kinetics and mechanics. *Am. Ceram. Soc. Bull.*, 1987, **66**(10), 1498–1504.
19. Smith, P. A., Kerch, H., Krueger, S., Long, G. G., Keller, J. and Haber, R. A., Pore sizes and filtration rates from two alumina slips. *J. Am. Ceram. Soc.*, 1994, **77**(7), 1777–1782.
20. Tiller, F. M. and Tsai, C., Theory of filtration of ceramics: I, slip casting. *J. Am. Ceram. Soc.*, 1986, **69**(12), 882–887.
21. Scherer, G. W., Theory of drying. *J. Am. Ceram. Soc.*, 1990, **73**(1), 3–14.
22. Salomoni, A., Galassi, C., Roncari, E., Stamenkovic, J. and Rastelli, E., Pressure casting of high-load alumina suspensions. In *Proceedings of 4th ECerS Conference*, Vol. 1, ed. C. Galassi. Gruppo Editoriale Faenza Editrice S. p. A., 1995, pp. 453–458.
23. Assmann, S., Eisele, U. and Böder, H., Processing of Al_2O_3/SiC composites in aqueous media. *J. Eur. Ceram. Soc.*, 1997, **17**, 309–317.
24. Nieto, M. I., Miranzo, P., de Aza, S. and Moya, J. S., Effect of atmosphere on microstructural evolution of pressureless sintered Al_2O_3/SiC composites. *J. Ceram. Soc. Jpn. Int. Ed.*, 1992, **100**, 464–467.
25. Anya, C. C. and Roberts, S. G., Pressureless sintering and elastic constants of Al_2O_3-SiC 'nanocomposites''. *J. Eur. Ceram. Soc.*, 1997, **17**, 564–573.
26. Aksay, I. A. and Schilling, C. H., Microstructure control through colloidal consolidation. In *Advances in Ceramics*, Vol. 9, *Forming of Ceramics*, ed. J. A. Mangels and G.L. Messing. Am. Ceram. Soc. Inc., 1984, pp. 94–104.
27. Zener, C., (quoted by C.S. Smith), Grains, phases and interfaces: an interpretation of microstructure. *Metals Technol.*, 1948, **15**(4) *Trans. AIME*, 175, 15–51.
28. Stearns, L. C. and Harmer, M. P., Particle-inhibited grain growth in Al_2O_3–SiC: I, experimental results. *J. Am. Ceram. Soc.*, 1996, **79**(12), 3013–3019.

29. Stearns, L. C. and Harmer, M. P., Particle-inhibited grain growth in Al_2O_3–SiC: II, Equilibrium and kinetic analysis. *J. Am. Ceram. Soc.*, 1996, **79**(12), 3020–3028.

30. Schmid, H. K., Aslan, M., Assmann, S., Naß, R. and Schmidt, H., Microstructural characterization of Al_2O_3/SiC nanocomposites. *J. Eur. Ceram. Soc.*, 1998, **18**, 39–49.

31. Zhao, J., Stearns, L. C., Harmer, M. P., Chan, H. M., Miller, G. A. and Cook, R. F., Mechanical behaviour of alumina–silicon carbide "nanocomposites". *J. Am. Ceram. Soc.*, 1993, **76**(2), 503–510.

32. Kara, H. and Roberts, S. G., Polishing behaviour and surface quality of alumina and alumina/silicon carbide nanocomposites. *J. Am. Ceram. Soc.*, 2000, **83**(5), 1219–1225.

33. Chiu, R. C., Garino, T. J. and Cima, M. J., Drying of granular films: I, effect of processing variables on cracking behaviour. *J. Am. Ceram. Soc.*, 1993, **76**(9), 2257–2264.